Available online at www.sciencedirect.com

ScienceDirect

Ceramics International 39 (2013) 9835–9844

CERAMICS INTERNATIONAL

www.elsevier.com/locate/ceramint

Phase transformation, microstructural and mechanical properties of hydroxyapatite/alumina nanocomposite scaffolds produced by freeze casting

Seyed Mohammad Hossein Ghazanfari, Ali Zamanian*

Nanotechnology & Advanced Materials Department, Materials & Energy Research Center, P.O. Box: 13145-1659, Karaj, Iran

Received 7 February 2013; received in revised form 25 May 2013; accepted 27 May 2013
Available online 31 May 2013

Abstract

Freeze casting is an effective fabrication technique that allows producing scaffolds with variable porosity, pore size, pore orientation and compressive strength. To our knowledge, the present study is the first investigation on the replacement effects of microparticles with nanoparticles in bone scaffolds prepared through the freeze casting method. In this study, the effect of nano-alumina content on phase transformation, microstructural and mechanical properties of hydroxyapatite/nano-alumina (HA/nAl_2O_3) nanocomposite scaffolds, fabricated through the freeze casting method at different cooling rates, has been investigated. In the first stage, slurries with 15 vol% solid loading and different nano-alumina content were prepared. In the next stage, cooling rates of 1 and 4 K/min were applied to synthesize the porous scaffolds, followed by sintering at 1250 and 1350 °C. The characteristics of the initial powders, and phase composition, microstructure, pore size, pore distribution and mechanical strength of the scaffolds were assessed. The porosity of the synthesized scaffolds was in a range of 78–85%, and the compressive strength varied from 0.2 to 4 MPa as a function of nAl_2O_3 concentration, cooling rate, and sintering temperature. Surprisingly, further addition of nAl_2O_3 not only affected the microstructural features, but also provided mechanisms to improve the mechanical strength of the scaffolds.

Keywords: Freeze casting; Ice templating; Hydroxyapatite; Nano-alumina; Scaffold

1. Introduction

Implantation of bone autografts or allografts is a simple strategy to heal large bone defects. However, there are some drawbacks of these strategies which limit their widespread usage, such as extended surgical time and donor site morbidity for autograft, and adverse immune response and pathogen disease transmission for allograft. These problems have guided researchers for the development of bone substitute materials [1–4].

As the most promising bone substitute materials, calcium phosphate (CP) compounds have been widely used clinically due to their similarity to hard tissues. Among different CP ceramics, hydroxyapatite (HA) and tri-calcium phosphate (TCP), or combinations of these two materials (biphasic ceramics) have gained special attentions for a wide range of applications such as alveolar ridge augmentation [5], maxillofacial reconstruction [6], orbital implants [7], spine fusion [8] and repair of bone defects [9]. These materials have been clinically used in dense, granular and porous forms [10–12]. It is known that the porous constructs of this class of materials have the possibility of tissue growth, and the capability of being replaced by bone tissue [13–15]. Unlikely, CPs have also some drawbacks such as relatively low mechanical strength (TCPs and biphasic materials) and thermal decomposition during the sintering [16,17]. Many materials such as zirconia [18], alumina [19], silica [20], titania [21] and calcium silicate [22] have been employed to overcome these drawbacks. Generally, porous alumina structures in comparison with porous CPs have better mechanical strength but due to the lack of appropriate cellular responses they cannot form biochemical interfacial bond with the natural tissue [23–25]. Therefore, it is reasonable to reinforce CP porous structures with alumina powder to fabricate highly bioactive nanocomposite scaffolds with a relatively higher mechanical strength.

*Corresponding author. Tel.: +98 912 3211180; fax: +98 26 36201888.
E-mail addresses: a-zamanian@merc.ac.ir, zamanian_a@yahoo.com (A. Zamanian).

0272-8842/$ - see front matter © 2013 Elsevier Ltd and Techna Group S.r.l. All rights reserved.
http://dx.doi.org/10.1016/j.ceramint.2013.05.096

Different fabrication techniques such as pore-foaming [26], infiltration of compression molded sponge [27], gel-casting [28], slip-casting [29], starch consolidation [30], microwave processing [31] and freeze casting [32,33] can be used for the production of porous structures. Among these techniques, freeze casting has gained much attention due to its superior advantages such as simplicity, low shrinkaging in forming process, possibility of controlling the porosity, interconnectivity, relatively good mechanical strength etc. [14,34,35]. Different additives have been also used to improve the properties of HA-based scaffolds fabricated via the freeze casting method. Recently, Zuo et al. [36] investigated the effect of polyvinyl alcohol (PVA) addition on the morphology of porous HA structures produced by freeze casting. According to their results the PVA-free HA structures showed longer lamellar pores. Zhang et al. [37] studied the effect of gelatin addition on the microstructure of freeze cast porous HA structures. They showed that the viscosity of HA slurry and also the linear shrinkage ratio of the sintered samples were enhanced by increasing the gelatin concentration. In another work, Blindow et al. [20] investigated the influence of nano SiO_2 addition on HA scaffolds produced via freeze casting. They found that SiO_2 addition announced a partial phase transformation of HA to β-TCP and reduced the shrinkage of the scaffolds after sintering. This interesting study could be completed by investigating the microstructural changes caused by further addition of nano SiO_2 to the HA scaffolds [20].

As mentioned above, different compositions, additives and fabrication techniques can significantly affect the microstructural and mechanical properties of freeze casted scaffolds. In our previous study, we have demonstrated that the freeze casted HA scaffolds exhibit relatively high mechanical properties [32]. To our knowledge, the influence of adding nanoparticles on the microstructural features of scaffolds, prepared by the freeze casting process, has not been fully investigated. The aim of this research is to study the influence of adding nano-alumina (nAl_2O_3) on the microstructure, mechanical properties, shrinkage and phase transformation of HA scaffolds fabricated by the freeze casting technique.

2. Materials and methods

2.1. Scaffolds fabrication

The HA/nAl_2O_3 nanocomposite scaffolds with 15 vol% solid concentration have been produced via an unidirectional freeze casting technique. At first, to prepare stable slurries, a small amount of dispersant agent (4 wt% of HA/nAl_2O_3 content) (Dolapix CE 64, Zschimmer & Schwarz, Lahnstein, Germany) has been added to distilled water. Then, different amounts of HA powder (2196, Merck KGaA, Darmstadt, Germany) and nano-alumina (Nabond, china, purity of 99.9%) have been added bit by bit to suspension, using high speed magnetic stirring, as shown in Table 1. The mean particle size (d50) and specific surface area were 1.69 μm and 75.81 m^2/g for HA, and 5 nm and 500–600 m^2/g for nano-alumina, respectively. All of these data were provided by the manufacturer. Then, the prepared slurries were ball-milled for 24 h with zirconia balls. After that, polyvinyl alcohol (PVA, $M_w = 15000$, Merck, Darmstadt, Germany) was added as a binder at 4 wt% of the HA/nAl_2O_3 content. Before casting, a vacuum oven was used for air bubble removal at a pressure of 0.02 MPa for 20 min.

The scaffolds were prepared using a custom-made setup as described previously [32]. Briefly, the slurries were poured into a PTFE mold, located on a cold finger, where the temperature was adjusted using liquid nitrogen and a heater connected to a PID controller. The slurries were poured into the PTFE mold at 5 °C, and different cooling rates were applied to solidify the samples (see Table 1). Then, the solidified samples were removed from the mold carefully and placed in a freeze dryer (FD-10, Pishtaz Engineering Co., Tehran, Iran) for 48 h to sublimate the ice crystals. After sublimation, the green bodies were sintered at different temperatures. All samples were heated to 600 °C at heating rate of 5 K/min and kept for 24 h at this temperature. The samples were then heated to the ultimate sintering temperatures at the same heating rate and maintained for 2 h. The sintering cycles were completed with a cooling rate of 300 K/h down to room temperature.

2.2. Property characterization

2.2.1. Phase analysis

Phase analysis of the sintered HA/nAl_2O_3 composite scaffolds was conducted using a X-ray diffraction (XRD, Philips PW3710) with monochromatic Cu-Kα radiation under the operating conditions of 40 kV and 30 mA. Comparison of XRD patterns with JCPDS standards was carried out to identify the crystalline phases.

Table 1
Slurry concentration, cooling rate and sintering temperature of samples.

Sample Code	A5C1T2	A5C1T3	A5C4T2	A5C4T3	A10C1T2	A10C1T3	A10C4T2	A10C4T3	A15C1T2	A15C1T3	A15C4T2	A15C4T3
Micro-HA content (vol%)	95	95	95	95	90	90	90	90	85	85	85	85
Nano-alumina content (vol%)	5	5	5	5	10	10	10	10	15	15	15	15
Cooling rate (K/min)	1	1	4	4	1	1	4	4	1	1	4	4
Sintering temperature (°C)	1250	1350	1250	1350	1250	1350	1250	1350	1250	1350	1250	1350

2.2.2. Microstructural characterization

The morphology of the nAl_2O_3 and HA particles was analyzed by transmission electron microscopy (TEM). For this purpose, the powders were ultrasonically dispersed in ethanol to form a diluted suspension and then a few droplets were dropped on carbon coated copper grids. The morphology of the particles was observed by a TEM instrument (GM200 PEG Philips), operated at an accelerating voltage of 200 kV. Also, scanning electron microscopy (SEM, Stereoscan S 360-Leica Cambridge, England) was used to characterize the morphology and the microstructure of the scaffolds. Before scanning, the scaffolds were coated by a thin layer of gold for a better electrical conductivity.

2.2.3. Porosity and pore size of scaffolds

The total porosity of the sintered scaffolds (P) was calculated by density measurement (ratio of weight to total volume, $\rho_{scaffold}$) and theoretical density (depending on the amount of HA and nAl_2O_3, ρ_{solid}) using [38]

$$P = 1 - \rho_{scaffold/}\ \rho_{solid} \quad (1)$$

At least five samples were calculated to obtain the average value and the standard deviation. Because the HA/nAl_2O_3 nanocomposites scaffolds were anisotropic, pore sizes were determined in both long and short axes. The pore sizes were measured using Quantify Image software and five samples were studied, with 50 measurements conducted for each sample.

2.2.4. Shrinkage measurement

The shrinkage volume was calculated using the sample's volume before and after sintering [39]:

$$S_V = (V_0 - V_f)/V_0 \quad (2)$$

where S_V, V_0 and V_f are the total shrinkage, initial and final volumes, respectively. At least five samples were calculated to obtain the average value and the standard deviation.

2.2.5. Mechanical testing

For the compressive strength measurements, the cylindrical scaffolds with diameters of 15 mm and heights of 20 mm were loaded with a cross-head speed of 0.5 mm/min using a screw-driven load frame (Instron 5565, Instron Corp., Canton, MA). The stress responses were monitored for at least five samples of each group with different HA/nAl_2O_3 contents to obtain the average values and the standard deviations.

3. Results and discussion

3.1. TEM diffraction

Fig. 1 demonstrates the TEM images of HA and nAl_2O_3 powders. Fig. 1(a) shows the TEM image of HA microparticles. As shown in Fig. 1(b), the nAl_2O_3 grains are extremely small and separated from each other.

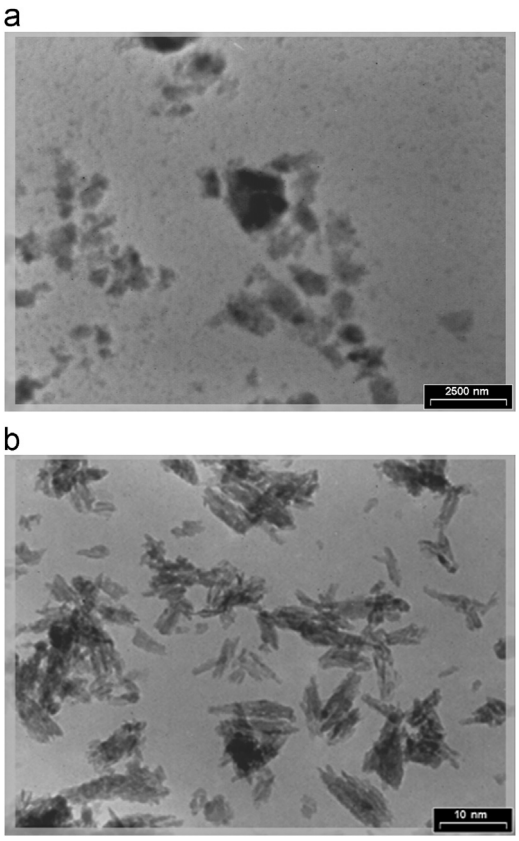

Fig. 1. TEM macrograph of (a) HA and (b) nAl_2O_3 powders.

3.2. Phase analysis

There are two main factors responsible for phase transformation study of HA/nAl_2O_3 nanocomposites. The first factor is the content of nAl_2O_3 in the samples. Fig. 2 (a1–d1) shows the XRD patterns of HA/nAl_2O_3 nanocomposites with different HA/nAl_2O_3 contents (and pure HA as the control) sintered at 1250 °C (A5C1T2, A10C1T2, A15C1T2). As shown in Fig. 2 (a1), HA was the only detectable phase and no secondary phase was found after sintering at 1250 °C. In the sample containing 5 vol% nAl_2O_3 (A5C1T2), the HA phase partially decomposed to TCP. When the volume percent of nAl_2O_3 increased, the phase transformation from HA to TCP increased and became completed for the sample containing 10 vol% nAl_2O_3 (A10C1T2). It has been reported that TCP is more biodegradable in comparison to HA [40], which is of interest for tissue engineering applications. In all the XRD patterns (A5C1T2, A10C1T2, and A15C1T2), no significant peak related to Al_2O_3 could be detected. The lack of alumina peaks in the XRD patterns obviously showed that Al_2O_3 reacted with HA and formed other phases. Additionally, some other peaks could be identified in the XRD patterns that belonged to $CaAl_2O_4$ (JCPDS#70-0134) and $CaAl_4O_7$ (JCPDS#74-1467) which were confirmed by other studies [41]. Usually, HA decomposes into TCP around 1350–1400 °C, as previously described by the reaction shown in Eq. (3) or in some studies with Eq. (4) [42,43]. However, HA/nAl_2O_3 nanocomposites are known

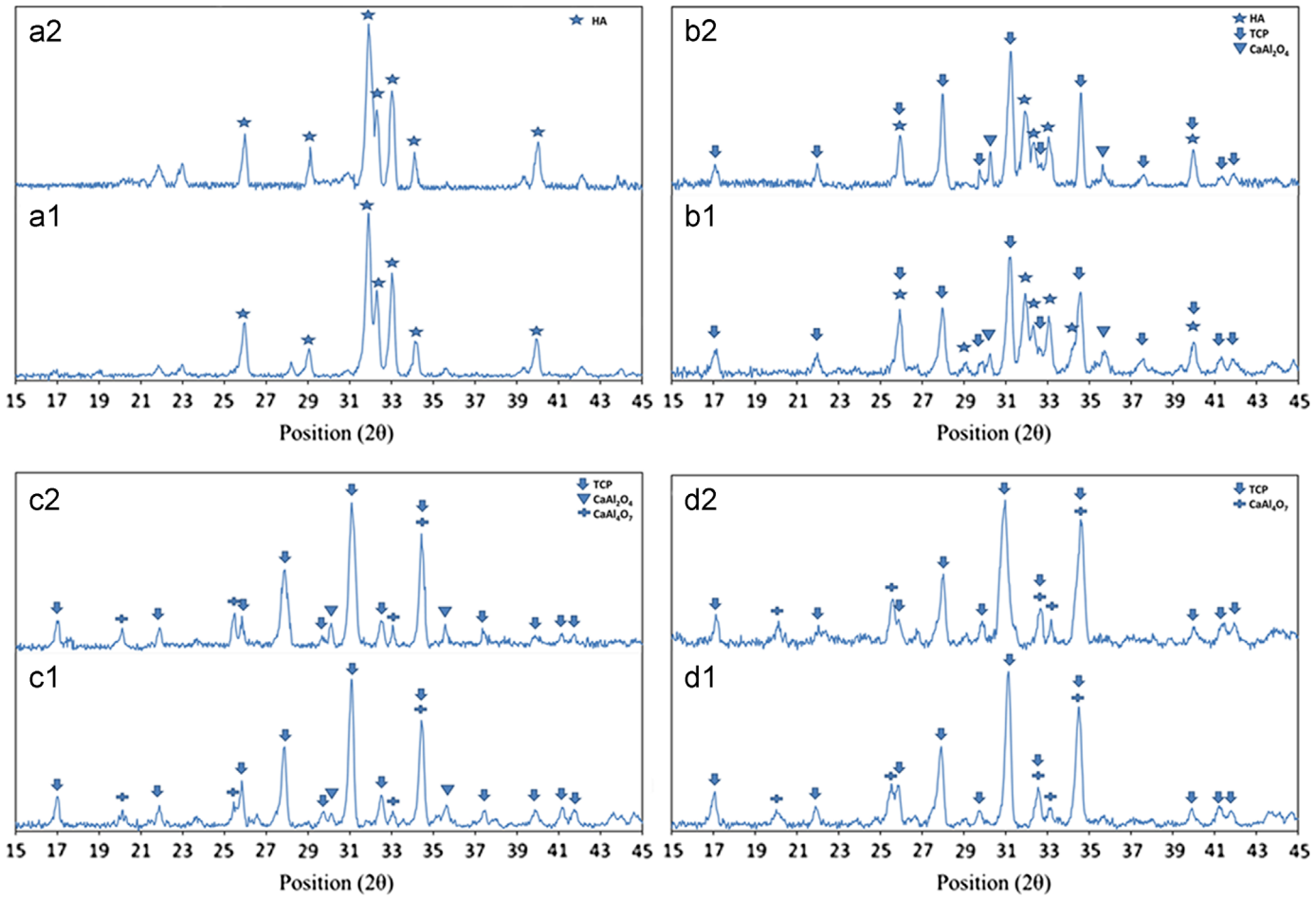

Fig. 2. XRD patterns of HA/nAl_2O_3 nanocomposites sintered at different temperatures ((a) Pure HA at 1250 °C and 1350 °C; (b) A5C1T2 and A5C1T3; (c) A10C1T2 and A10C1T3; and (d) A15C1T2 and A15C1T3).

to decompose at relatively low temperatures with the formation of calcium aluminates, as shown in Eq. (5):

$$Ca_{10}(PO_4)_6(OH)_2 \rightarrow 3Ca_3(PO_4)_2 + CaO + H_2O \quad (3)$$

$$Ca_{10}(PO_4)_6(OH)_2 \rightarrow 2Ca_3(PO_4)_2 + Ca_4P_2O_9 + H_2O \quad (4)$$

$$Ca_{10}(PO_4)_6(OH)_2 + Al_2O_3 \rightarrow 3Ca_3(PO_4)_2 + CaAl_2O_4 + H_2O \quad (5)$$

Also, the formation of calcium aluminates can be related to the reaction shown in Eq. (6). This means that CaO (calcium oxide), made by HA decomposition, reacted with alumina to form calcium aluminates [41,44,45].

$$nCaO + mAl_2O_3 \rightarrow Ca_nAl_{2m}O_{3m+n} \quad (6)$$

It was observed that increasing the nAl_2O_3 content in the slurry leaded in diminishing of calcium aluminate with low content of aluminum ($CaAl_2O_4$) and instead, formation of calcium aluminate with more content of aluminum ($CaAl_4O_7$). It is worth mentioning that Eq. (6) could truly confirm these observations. The second factor is the sintering temperature. Fig. 2 (a2–d2) shows the XRD patterns of the HA/nAl_2O_3 nanocomposites with different HA/nAl_2O_3 contents (and pure HA as the control) sintered at 1350 °C (A5C1T3, A10C1T3, A15C1T3). All the phase transformations of the HA/nAl_2O_3 nanocomposites in this temperature are the same as the samples sintered at 1250 °C, only with different intensities. Fig. 2(a) compares the XRD patterns of the pure HA in two different sintering temperatures. As can be seen, HA was the only phase in both patterns and no secondary phases could be found after sintering in these temperatures. However, according to Fig. 2(b–d), it is completely obvious that increasing the temperature accelerates the HA decomposition and calcium aluminates formation in all samples.

3.3. Microstructural characterization

Figs. 3 and 4 show the horizontal and vertical cross section SEM micrographs of HA/nAl_2O_3 composites, respectively, including different nAl_2O_3 contents at different cooling rates (1 and 4 K/min). As it can be seen, two factors have significant effects on the microstructure of HA/nAl_2O_3 nanocomposite scaffolds as cooling rate and particle size. The pore size and wall thickness can be adjusted frequently by increasing or decreasing the cooling rate during the freezing process, as previously reported by many researchers [14,34,46]. Figs. 3 and 4 obviously show that increasing of cooling rate provides smaller pores and thinner walls. Higher cooling rate means

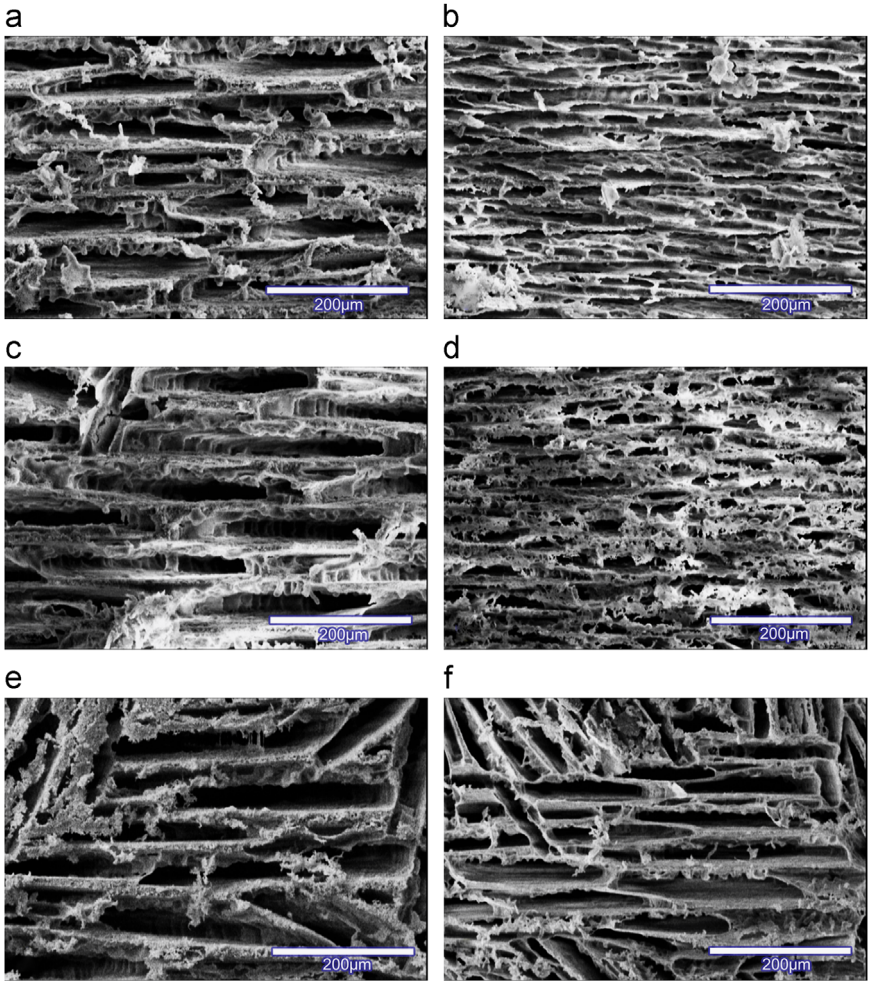

Fig. 3. Horizontal cross section SEM micrographs of HA/nAl_2O_3 nanocomposites at different cooling rates ((a) HA/5% nAl_2O_3, (c) HA/10% nAl_2O_3 and (e) HA/15% nAl_2O_3 all at 1 K/min; (b) HA/5% nAl_2O_3, (d) HA/10% nAl_2O_3 and (f) HA/15% nAl_2O_3 all at 4 K/min).

higher interface velocity (ν) and thinner structural wavelength (λ) [average ice crystal thickness+entrapped particles thickness, see Fig. 5(a)] [47], and consequently finer lamellae structure according to

$$\lambda \sim \nu^{-n} \tag{7}$$

where λ is structural wavelength, ν is velocity of ice front, and n depends on particle size [47]. On the one hand, at the cooling rate of 4 K/min, compared to the cooling rate of 1 K/min, the water in the slurry reaches a supercooled state more quickly, and then higher amounts of ice crystals are formed [34]. Due to the quick freezing time, the ice crystal growth is repressed and the smaller crystals are formed. In addition, at the cooling rate of 4 K/min, compared to the cooling rate of 1 K/min, the particles have less time to migrate and rearrange by diffusion mechanisms that consequently cause formation of thinner walls. Generally, the narrower structures could be obtained by increasing the cooling rate.

As it can be seen in Figs. 3 and 4, the pore size and wall thickness could be attuned by replacing the microsize particles with the nanosize particles. As previously described [48], the larger particle size results in finer lamellar structures [Fig. 5(b)], which is in a good agreement with the obtained results about the composite containing nano- and micro-particles. In fact, increasing the particle size leads to increasing n and ν parameters [47,48] and decreasing the structural wavelength according to Eq. (7), and consequently finer lamellar structures. The increasing of ν is due to the larger particles that in this case means smaller surface area. This smaller surface area provides few nucleation sites and simultaneously reduces initial temperature for nucleation [48]. So, the system enters in progressively supercooled state which causes a faster interface velocity. In turn, the larger particles have less time for reordering between the ice crystals, and thereby thinner walls are produced. According to our previous study, hollow spaces remain between larger particles in comparison with smaller particles (see Zamanian et al. Fig. 7 Ref. [49]). As shown in Figs. 5(b) and 6, the nanoparticles fill these inter-particle spaces and the walls become denser, that can influence mechanical strength.

3.4. Evaluation of mechanical strength

Table 2 shows the values of shrinkage, porosity, compressive strength and pore size of all samples. The effective parameters for the mechanical strength of the scaffolds can

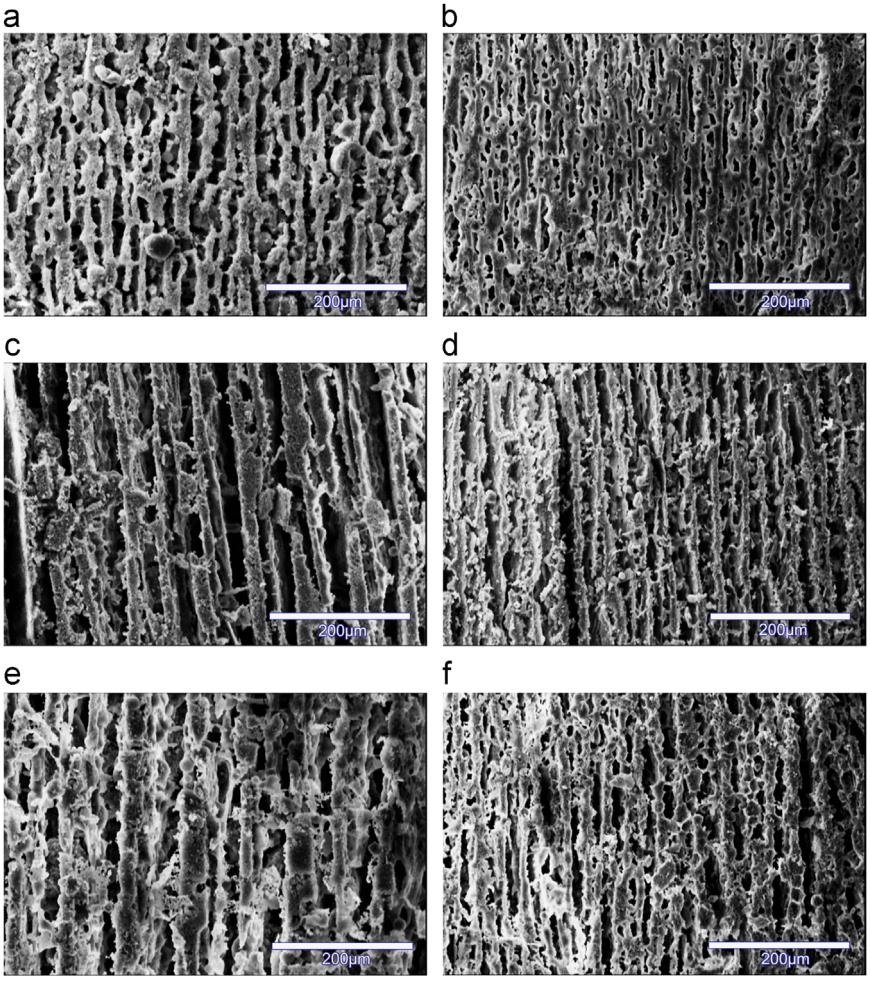

Fig. 4. Vertical cross section SEM micrographs of HA/nAl_2O_3 nanocomposites at different cooling rates ((a) HA/5% nAl_2O_3, (c) HA/10% nAl_2O_3 and (e) HA/15% nAl_2O_3 all at 1 K/min; (b) HA/5% nAl_2O_3, (d) HA/10% nAl_2O_3 and (f) HA/15% nAl_2O_3 all at 4 K/min).

be found in all the processing steps: slurry formulation and preparation (HA/nAl_2O_3 percentage), solidification (cooling rate) and sintering. By varying the processing parameters, properties such as porosity and pore size, density and thickness of the walls, shrinkage percentage and phase composition of final scaffolds can be controlled [32,34]. Fig. 7 shows pore size, porosity, shrinkage and mechanical strength of the scaffolds as a function of nAl_2O_3 content. Obviously, the total porosity value decreases with increasing the nAl_2O_3 contents. This is due to increasing in volume shrinkage and dense walls, as mentioned above in Section 3.3. Also, it is clear that the compressive strength of the scaffolds augments with increasing the nAl_2O_3 contents [41,45]. The formation of calcium aluminate phases in the TCP matrix as well as decreasing the porosity can be the reasons of this improvement in the compressive strength. It is worth mentioning that Al_2O_3 is one of the most widely used reinforcement materials for HA composites that causes significant increment in the compressive strength values as a result of calcium aluminate formation [41,50,51]. As it can be seen in Fig. 7, the pore sizes and also compressive strength increased with multiplying nAl_2O_3 content, while it has been widely stated that compressive strength decreases by increasing pore size [46,52].

It is well known that porosity and pore size plays an important role on initial cell adhesion, cell ingrowth and blood vascularization. Murphy et al. [53] showed that the increased surface area provided by the scaffolds with smaller pore size may have a beneficial effect in initial cell adhesion, but ultimately the improved cellular infiltration provided by scaffolds with larger pores outweighs this effect. They indicated that an early additional peak in cell number could be seen in the scaffolds with a mean pore size of 120 µm and then this early peak disappeared following the cell proliferation. They observed that the scaffolds with pores about 300 µm had a better cell migration behavior. Thus, different pore size ranges are required for good vascularization and cell ingrowth. On the other hand both length and width of the pores are important for appropriate cell ingrowth. Therefore, as can be seen in Fig. 7, further increase in pore width is desirable for the scaffolds.

Another important factor that influences the compressive strength is cooling rate. As it can be seen in Fig. 8, by increasing the cooling rate from 1 K/min to 4 K/min, the compressive strength relatively increased. With an increase in the cooling rate, the pore size decreased because of the higher interface velocity (shorter freezing time), and as a result an

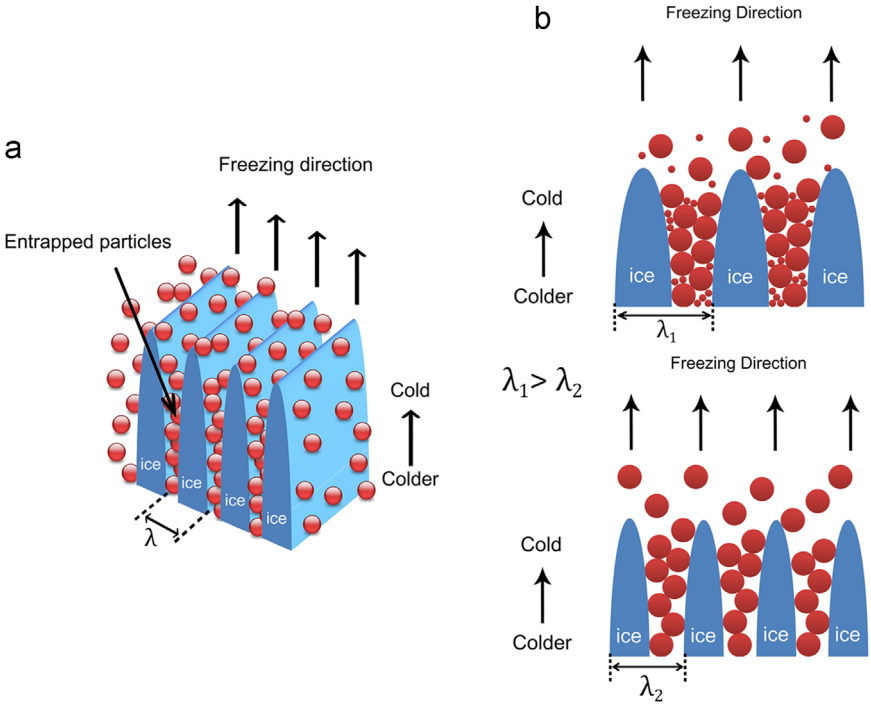

Fig. 5. (a) 3D schematic image of ice formation and particles entrapment during the freeze casting process and (b) 2D schematic image of influence of nAl_2O_3 addition on ice formation, particles entrapment and structural wavelength (λ).

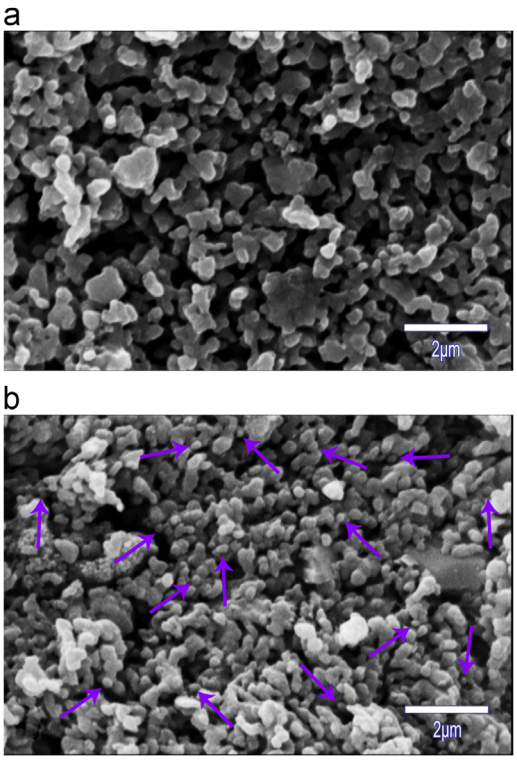

Fig. 6. SEM micrographs of inter-particle spaces filled with nanoparticles ((a) HA/5% nAl_2O_3 and (b) HA/15% nAl_2O_3). Arrows indicate nanoparticles in the matrix.

improvement in the compressive strength of the nanocomposite scaffolds was observed. Our results related to the relationship between the cooling rate and the compressive strength is in a good agreement with the reported data by other researchers [32,34].

As shown in Fig. 9, the shrinkage and the compressive strength increased as a function of sintering temperature while the sintering temperature had an opposite effect on the total porosity. According to the literature, when the sintering temperature increases from 1250 to 1350 °C, the porosity goes down and the shrinking value goes up, and as a result the compressive strength increases [32,34]. In a recent study, Sopyan et al. [54] fabricated HA/alumina scaffolds via the protein foaming consolidation method and obtained compressive strength and porosity values of 0.1 MPa and 45.2%, respectively, after addition of 50% alumina. In another work, An et al. [18] used zirconia to improve the mechanical strength of HA scaffolds, produced by the polymer sponge method, and obtained a compressive strength of near 3 MPa and porosity around 80% by even adding 60% zirconia to the HA matrix. In total, optimal compressive strengths for this type of scaffolds can be obtained by controlling the nano-alumina content and cooling rate. Although, more desirable results were achieved compared to the reported data by other researchers at the nearly same porosity [18,54], these samples are not still appropriate to be used in load bearing sites [55]. According to the previous studies, there might be some bridges between lamellar pores that could improve the mechanical properties of the structure [47,56]. However, the formation mechanism and characteristics of these bridges have not been completely understood, and there are inadequate data in the available articles. The ability to manipulate these bridges would be expected to achieve engineered scaffold constructs with better mechanical properties.

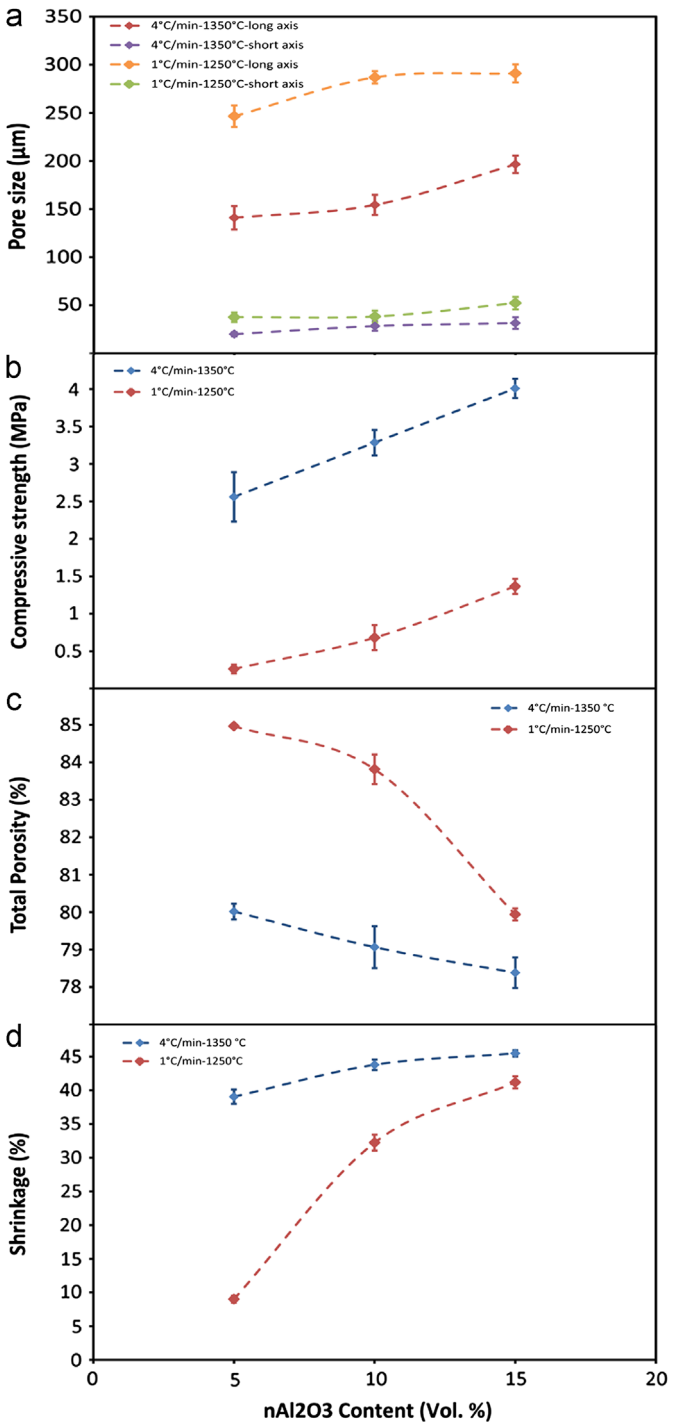

Fig. 7. Effect of nAl_2O_3 content on pore size (a), compressive strength (b), porosity (c) and shrinkage (d) of HA/nAl_2O_3 nanocomposites.

Table 2
The shrinkage, porosity, compressive strength and pore size of samples.

Sample code	Shrinkage (%)	Porosity (%)	Compressive strength (MPa)	Pore size—long (µm)	Pore size—short (µm)
A5C1T2	9.01	84.96	0.263	246.55	37.51
A5C1T3	39.04	79.36	1.556	218.45	33.2
A5C4T2	10.81	84.45	0.268	161.26	22.44
A5C4T3	39.33	80.01	2.559	140.87	19.83
A10C1T2	32.23	83.81	0.68	286.97	38.19
A10C1T3	43.78	79.16	1.547	272.56	36.15
A10C4T2	31.46	82.59	0.922	164.62	30.24
A10C4T3	44.22	79.06	3.284	154.25	28.25
A15C1T2	41.17	79.94	1.365	291.02	52.14
A15C1T3	45.48	78.73	2.047	285.07	50.12
A15C4T2	40.62	80.37	2.209	201.73	32.96
A15C4T3	45.16	78.38	4.007	196.55	31.32

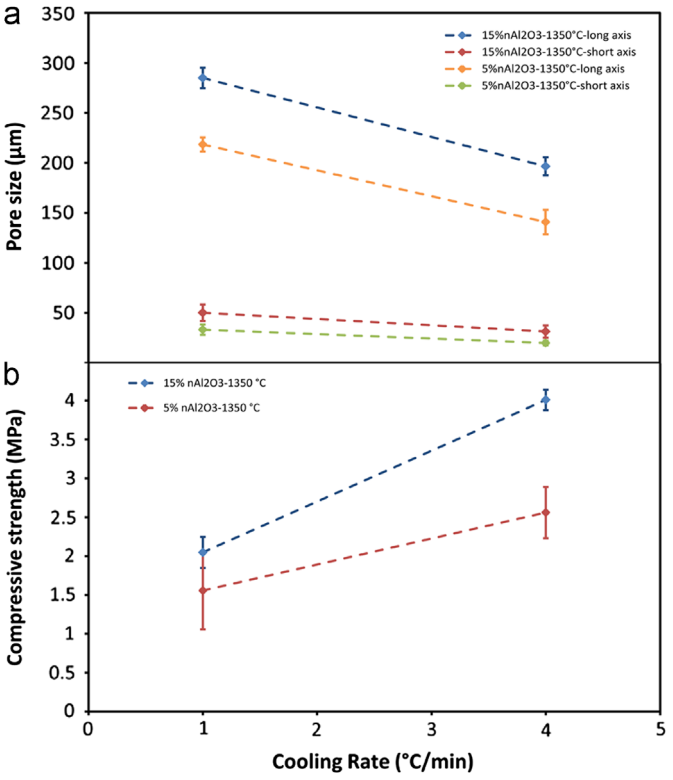

Fig. 8. Effect of cooling rate on pore size (a) and compressive strength (b) of HA/nAl_2O_3 nanocomposites.

4. Conclusions

In this study, the effect of further addition of nano-alumina particles to HA-based scaffolds on the microstructural, phase transformation and mechanical properties as well as sintering behavior of porous HA/nAl_2O_3 scaffolds has been evaluated. The obtained results showed that by increasing the nAl_2O_3 content and sintering temperature, the decomposition of HA to TCP was accelerated. In addition, increasing the nAl_2O_3 content led to increasing the pore size and the compressive strength of the scaffolds. The formation of calcium aluminate phases caused increasing of the walls' densities and thicknesses as well as decreasing of the porosity, which might be the reason of this improvement in the compressive strength. By manipulating the nAl_2O_3 content, the cooling rate and sintering temperature, the scaffolds with total porosities between 78% and 85% and compressive strengths from 0.2 to 4 MPa were achieved. Finally, the results showed that the pore size, porosity and compressive strength could be attuned by

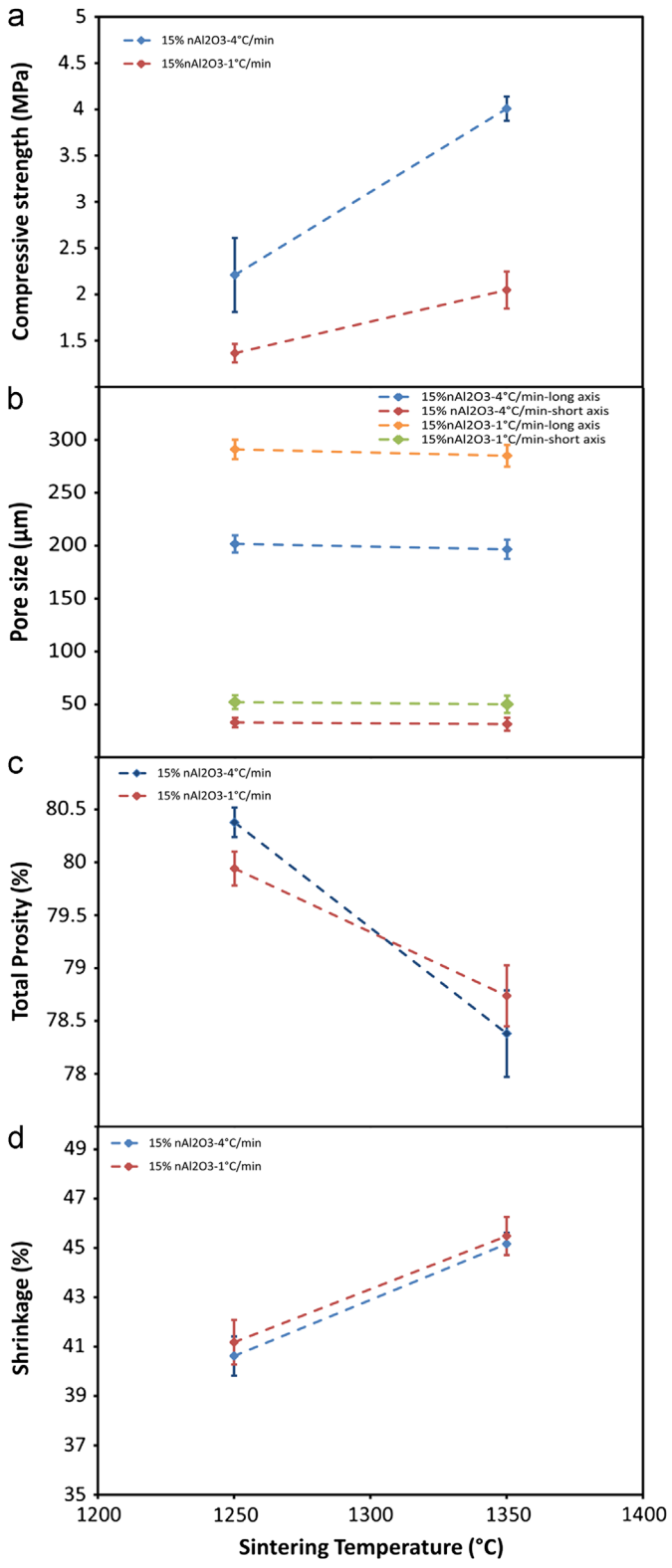

Fig. 9. Effect of sintering temperature on compressive strength (a), pore size (b), porosity (c) and shrinkage (d) of HA/nAl_2O_3 nanocomposite scaffolds.

adjusting the ratio of microparticles to nanoparticles content in the freeze casting process. Since the ice volume, the size and morphology of the ice crystals can be influenced by using different additives in the initial suspension, more extensive studies on the effect of additives such as different anti-freezing agents, binders and dispersants need to be designed for the improvement of the scaffold properties. The favorable mechanical behavior coupled with the ability to modify the microstructures shows the potential of the freeze casting technique for the synthesis of excellent bone tissue engineering scaffolds.

References

[1] K. Arvidson, B.M. Abdallah, L.A. Applegate, N. Baldini, E. Cenni, E.G. Barrena, D. Granchi, M. Kassem, Y.T. Konttinen, K. Mustafa, D.P. Pioletti, T. Sillat, A.F. Wistrand, Bone regeneration and stem cells, Journal of Cellular and Molecular Medicine 15 (4) (2011) 718–746.

[2] M. Yasaei, A. Zamanian, F. Moztarzadeh, M. Ghaffari, M. Mozafari, Characteristics improvement of calcium hydroxide dental cement by hydroxyapatite nanoparticles. Part 1: formulation and microstructure, Biotechnology and Applied Biochemistry, http://dx.doi.org/10.1002/bab.1119, in press.

[3] M. Jafarkhani, A. Fazlali, F. Moztarzadeh, M. Mozafari, Mechanical and structural properties of polylactide/chitosan scaffolds reinforced with nano calcium phosphate, Iranian Polymer Journal 10 (2012) 713–720.

[4] P. Holzmann, E. Niculescu-Morzsa, H. Zwickl, F. Halbwirth, M. Pichler, M. Matzner, F. Gottsauner-Wolf, S. Nehrer, Investigation of bone allografts representing different steps of the bone bank procedure using the CAM-model, Altex 27 (2) (2010) 97–103.

[5] M. Jafarkhani, A. Fazlali, F. Moztarzadeh, Z. Moztarzadeh, M. Mozafari, Fabrication and characterization of PLLA/chitosan/nano calcium phosphate scaffolds by freeze casting technique, Industrial and Engineering Chemistry Research 51 (2012) 9241–9249.

[6] S.E. Lobo, T.L. Arinzeh, Biphasic calcium phosphate ceramics for bone regeneration and tissue engineering applications, Materials 3 (2) (2010) 815–826.

[7] R.Z. LeGeros, Calcium phosphates in oral biology and medicine, Monographs in Oral Science 15 (1991) 1–201.

[8] S. Dorozhkin, Medical application of calcium orthophosphate bioceramics, BIO 1 (1) (2011) 1–51.

[9] F.D. Burstein, S.R. Cohen, R. Hudgins, W. Boydston, C. Simms, The use of hydroxyapatite cement in secondary craniofacial reconstruction, Plastic and Reconstructive Surgery 104 (5) (1999) 1270–1275.

[10] P. Korovessis, M. Repanti, G. Koureas, Does coralline hydroxyapatite conduct fusion in instrumented posterior spine fusion?, Studies in Health Technology and Informatics 91 (2002) 109–113

[11] S.V. Dorozhkin, Amorphous calcium (ortho)phosphates, Acta Biomaterialia 6 (12) (2010) 4457–4475.

[12] I. Sato, T. Akizuki, S. Oda, H. Tsuchioka, C. Hayashi, A.A. Takasaki, K. Mizutani, N. Kawakatsu, A. Kinoshita, I. Ishikawa, Y. Izumi, Histological evaluation of alveolar ridge augmentation using injectable calcium phosphate bone cement in dogs, Journal of Oral Rehabilitation 36 (10) (2009) 762–769.

[13] M. Oates, R. Chen, M. Duncan, J.A. Hunt, The angiogenic potential of three-dimensional open porous synthetic matrix materials, Biomaterials 28 (25) (2007) 3679–3686.

[14] S. Deville, Freeze casting of porous biomaterials: structure, properties and opportunities, Materials 3 (3) (2010) 1913–1927.

[15] A. Hamlekhan, F. Moztarzadeh, M. Mozafari, M. Azami, N. Nezafati, Preparation of laminated poly(ε-caprolactone)-gelatin–hydroxyapatite nanocomposite scaffold bioengineered via compound techniques for bone substitution, Biomatter 1 (2011) 1–11.

[16] I. Sopyan, M. Mel, S. Ramesh, K.A. Khalid, Porous hydroxyapatite for artificial bone applications, Science and Technology of Advanced Materials 8 (1–2) (2007) 116–123.

[17] F. Baghbani, F. Moztarzadeh, A. Gafari Nazari, A.H. Razavi Kamran, F. Tondnevis, N. Nezafati, M. Gholipourmalekabadi, M. Mozafari, Biological response of biphasic hydroxyapatite/tricalcium phosphate scaffolds intended for low load-bearing orthopaedic applications, Advanced Composites Letters 21 (2012) 16–24.

[18] S.H. An, T. Matsumoto, H. Miyajima, A. Nakahira, K.H. Kim, S. Imazato, Porous zirconia/hydroxyapatite scaffolds for bone reconstruction, Dental Materials 28 (12) (2012) 1221–1231.
[19] S. Kalmodia, S. Goenka, T. Laha, D. Lahiri, B. Basu, K. Balani, Microstructure, mechanical properties, and in vitro biocompatibility of spark plasma sintered hydroxyapatite–aluminum oxide–carbon nanotube composite, Materials Science and Engineering C 30 (8) (2010) 1162–1169.
[20] S. Blindow, M. Pulkin, D. Koch, G. Grathwohl, K. Rezwan, Hydroxyapatite/SiO_2 composites via freeze casting for bone tissue engineering, Advanced Engineering Materials 11 (11) (2009) 875–884.
[21] E. Fidancevska, G. Ruseska, J. Bossert, Y.M. Lin, A.R. Boccaccini, Fabrication and characterization of porous bioceramic composites based on hydroxyapatite and titania, Materials Chemistry and Physics 103 (1) (2007) 95–100.
[22] S. Sprio, A. Tampieri, G. Celotti, E. Landi, Development of hydroxyapatite/calcium silicate composites addressed to the design of load-bearing bone scaffolds, Journal of the Mechanical Behavior of Biomedical Materials 2 (2) (2009) 147–155.
[23] B.-H. Yoon, W.-Y. Choi, H.-E. Kim, J.-H. Kim, Y.-H. Koh, Aligned porous alumina ceramics with high compressive strengths for bone tissue engineering, Scripta Materialia 58 (7) (2008) 537–540.
[24] L.L. Hench, Bioceramics: research and development opportunities, Brazilian Journal of Physics 22 (1992) 70–84.
[25] J.S. Magdeski, The porosity dependence of mechanical properties of sintered alumina, Journal of the University of Chemical Technology and Metallurgy 45 (2010) 143–148.
[26] K.H. Zuo, Y. Zhang, Y.P. Zeng, D. Jiang, Pore-forming agent induced microstructure evolution of freeze casted hydroxyapatite, Ceramics International 37 (1) (2011) 407–410.
[27] S.F. Corbin, X. Zhao-jie, H. Henein, P.S. Apte, Functionally graded metal/ceramic composites by tape casting, lamination and infiltration, Materials Science and Engineering A 262 (1–2) (1999) 192–203.
[28] G. Meng, H. Wang, W. Zheng, X. Liu, Preparation of porous ceramics by gelcasting approach, Materials Letters 45 (2000) 224–227.
[29] Y. Zhang, Y. Yokogawa, X. Feng, Y. Tao, Y. Li, Preparation and properties of bimodal porous apatite ceramics through slip casting using different hydroxyapatite powders, Ceramics International 36 (1) (2010) 107–113.
[30] A. Diaz, S. Hampshire, Characterisation of porous silicon nitride materials produced with starch, Journal of the European Ceramic Society 24 (2) (2004) 413–419.
[31] D.K. Agrawal, Microwave processing of ceramics, Current Opinion in Solid State and Materials Science 3 (1998) 480–485.
[32] S. Farhangdoust, A. Zamanian, M. Yasaei, M. Khorami, The effect of processing parameters and solid concentration on the mechanical and microstructural properties of freeze casted macroporous hydroxyapatite scaffolds, Materials Science and Engineering C 33 (1) (2013) 453–460.
[33] N. Arabi, A. Zamanian, Effect of cooling rate and gelatin concentration on the microstructural and mechanical properties of ice template gelatin scaffolds, Biotechnology and Applied Biochemistry (2013) http://dx.doi.org/10.1002/bab.1120.
[34] S. Deville, E. Saiz, A.P. Tomsia, Freeze casting of hydroxyapatite scaffolds for bone tissue engineering, Biomaterials 27 (32) (2006) 5480–5489.
[35] S. Deville, Freeze casting of porous ceramics: a review of current achievements and issues, Advanced Engineering Materials 10 (3) (2008) 155–169.
[36] K.H. Zuo, Y. Zeng, D. Jiang, Effect of cooling rate and polyvinyl alcohol on the morphology of porous hydroxyapatite ceramics, Materials and Design 31 (6) (2010) 3090–3094.
[37] Y. Zhang, K. Zuo, Y.P. Zeng, Effects of gelatin addition on the microstructure of freeze cast porous hydroxyapatite ceramics, Ceramics International 35 (6) (2009) 2151–2154.
[38] K.K. Mallick, Freeze casting of porous bioactive glass and bioceramics, Journal of the American Ceramic Society 92 (2009) S85–S94.
[39] A. Heunisch, A. Dellert, A. Roosen, Effect of powder, binder and process parameters on anisotropic shrinkage in tape cast ceramic products, Journal of the European Ceramic Society 30 (16) (2010) 3397–3406.
[40] G. Hannink, J.J. Arts, Bioresorbability, porosity and mechanical strength of bone substitutes: what is optimal for bone regeneration?, Injury, International Journal of the Care of the Injured 42 (Suppl 2) (2011) S22–25.
[41] H. Ji, P.M. Marquis, Preparation and characterization of Al_2O_3 reinforced hydroxyapatite, Biomaterials 13 (1992) 744–748.
[42] G. Muralithran, S. Ramesh, The effects of sintering temperature on the properties of hydroxyapatite, Ceramics International 26 (2000) 221–230.
[43] C.J. Liao, F.H. Lin, K.S. Chen, J.S. Sun, Thermal decomposition and reconstitution of hydroxyapatite in air atmosphere, Biomaterials 20 (1999) 1807–1813.
[44] H.W. Kim, Y.H. Koh, S.B. Seo, H.E. Kim, Properties of fluoridated hydroxyapatite–alumina biological composites densified with addition of CaF_2, Materials Science and Engineering C 23 (4) (2003) 515–521.
[45] Z. Evis, R.H. Doremus, A study of phase stability and mechanical properties of hydroxylapatite–nanosize α-alumina composites, Materials Science and Engineering C 27 (3) (2007) 421–425.
[46] K. Zhao, Y.F. Tang, Y.S. Qin, J.Q. Wei, Porous hydroxyapatite ceramics by ice templating: freezing characteristics and mechanical properties, Ceramics International 37 (2) (2011) 635–639.
[47] S. Deville, E. Saiz, A.P. Tomsia, Ice-templated porous alumina structures, Acta Materialia 55 (6) (2007) 1965–1974.
[48] S. Deville, E. Maire, A. Lasalle, A. Bogner, C. Gauthier, J. Leloup, C. Guizard, Influence of particle size on ice nucleation and growth during the ice-templating process, Journal of the American Ceramic Society 93 (9) (2010) 2507–2510.
[49] A. Zamanian, S. Farhangdoust, M. Yasaei, M. Khorami, M. Hafezi, The effect of particle size on the mechanical and microstructural properties of freeze casted macroporous hydroxyapatite scaffolds, International Journal of Applied Ceramic Technology (2013)http://dx.doi.org/10.1111/ijac.12031.
[50] P.M.M. Huaxia Ji, Sintering behavior of hydroxyapatite reinforced with 20 wt% Al_2O_3, Journal of Materials Science 28 (1993) 1941–1945.
[51] H.Y. Juang, M.H. Hon, Fabrication and mechanical properties of hydroxyapatite–alumina composites, Materials Science and Engineering C 2 (1994) 77–81.
[52] G. Tripathi, B. Basu, A porous hydroxyapatite scaffold for bone tissue engineering: physico-mechanical and biological evaluations, Ceramics International 38 (1) (2012) 341–349.
[53] C.M. Murphy, M.G. Haugh, F.J. O'Brien, The effect of mean pore size on cell attachment, proliferation and migration in collagen–glycosaminoglycan scaffolds for bone tissue engineering, Biomaterials 31 (3) (2010) 461–466.
[54] I. Sopyan, A. Fadli, M. Mel, Porous alumina–hydroxyapatite composites through protein foaming-consolidation method, Journal of the Mechanical Behavior of Biomedical Materials 8 (2012) 86–98.
[55] A.J. Wagoner Johnson, B.A. Herschler, Review of the mechanical behavior of CaP and CaP/polymer composites for applications in bone replacement and repair, Acta biomaterialia 7 (2011) 16–30.
[56] U.G. Wegst, M. Schecter, A.E. Donius, P.M. Hunger, Biomaterials by freeze casting, Philosophical Transactions of the Royal Society A 368 (1917) (2010) 2099–2121.